Biochimica et Biophysica Acta 1818 (2012) 839–850

Contents lists available at SciVerse ScienceDirect

Biochimica et Biophysica Acta

journal homepage: www.elsevier.com/locate/bbamem

Reconstitution of water channel function and 2D-crystallization of human aquaporin 8

Maria Agemark [a], Julia Kowal [b], Wanda Kukulski [b,1], Kristina Nordén [a], Niklas Gustavsson [a], Urban Johanson [a], Andreas Engel [b,*,2], Per Kjellbom [a,**]

[a] Center for Molecular Protein Science, Department of Biochemistry and Structural Biology, Lund University, P.O. Box 124, SE-221 00 Lund, Sweden
[b] Center for Cellular Imaging and Nano Analytics, Biozentrum, University of Basel, Mattenstrasse 26, CH-4002 Basel, Switzerland

ARTICLE INFO

Article history:
Received 26 May 2011
Received in revised form 25 November 2011
Accepted 6 December 2011
Available online 13 December 2011

Keywords:
Heterologous expression
AQP8
Aquaporin
2D crystallization

ABSTRACT

Among the thirteen human aquaporins (AQP0-12), the primary structure of AQP8 is unique. By sequence alignment it is evident that mammalian AQP8s form a separate subfamily distinct from the other mammalian aquaporins. The constriction region of the pore determining the solute specificity deviates in AQP8 making it permeable to both ammonia and H_2O_2 in addition to water. To better understand the selectivity and gating mechanism of aquaporins, high-resolution structures are necessary. So far, the structure of three human aquaporins (HsAQP1, HsAQP4, and HsAQP5) have been solved at atomic resolution. For mammalian aquaporins in general, high-resolution structures are only available for those belonging to the water-specific subfamily (including HsAQP1, HsAQP4 and HsAQP5). Thus, it is of interest to solve structures of other aquaporin subfamily members with different solute specificities. To achieve this the aquaporins need to be overexpressed heterologously and purified. Here we use the methylotrophic yeast *Pichia pastoris* as a host for the overexpression. A wide screen of different detergents and detergent–lipid combinations resulted in the solubilization of functional human AQP8 protein and in well-ordered 2D crystals. It also became evident that removal of amino acids constituting affinity tags was crucial to achieve highly ordered 2D crystals diffracting to 3 Å.

1. Introduction

Aquaporins (AQPs) are integral membrane proteins found in bacteria, eukaryotes and archaea. They function as passive protein channels for water [1] and some isoforms are also permeable to other small solutes such as urea, glycerol [2] and metalloids like arsenite, antimonite [3], boric acid [4] and silicic acid [5] in addition to water. Thirteen *Homo sapiens* isoforms (HsAQP0-12) expressed in different organs, cell types and subcellular locations have been identified [6]. Studies have shown that mutations in aquaporins are closely associated with human diseases [6,7]. When knockout mice are used as a model system a lack of obvious phenotype is sometimes seen when AQP genes are knocked out [8], maybe due to compensatory gene regulation, i.e. resulting in similar AQP isoforms taking over the function of the knocked AQP. In some cases a stress on the organism is necessary in order to discern the knockout phenotype [8]. Mice AQP1-5 have been reported to have multiple phenotypic abnormalities while AQP8-null mice were reported to only have a mild phenotype (hypertriglyceridemia) [8]. The aquaporins function in vivo as homotetramers, however each monomer has a pore. Individual monomers (26–34 kDa) have six transmembrane helices and five loops. Loops B and E contain the highly conserved asparagine–proline–alanine (NPA) motifs (Fig. 1a). Half helices formed by these loops are the hallmark of the AQP fold. The structures of human AQP1 [9] and of the *Escherichia coli* glycerol facilitator GlpF [10] revealed that the prolines belonging to the NPA motifs stack by van der Waals interactions in the middle of the membrane. The N-termini of the two half helices, HB and HE, meet at this point in the middle of the membrane. The dipoles of the two half helices generate a significant electrostatic barrier at the NPA region, which efficiently inhibits the permeation of protons [11,12]. Another conserved structure in the pore is the constriction region, also called the aromatic/arginine (ar/R) region, where 4 amino acids constitute a size restriction filter [12].

The first structure of a human AQP was solved by electron crystallography [9] and verified the hour glass model suggested by Jung et al. [13] more than 5 years earlier. Until now, mammalian AQP0 [14–16], AQP1 [9,12], AQP2 [17], AQP4 [18,19], AQP5 [20], plant SoPIP2;1 [21,22], bacterial AQPZ [23,24] and GlpF [10], the archaeal AQPM [25], the malarial parasite PfAQP [26], and the *Pichia pastoris* Aqy1

* Correspondence to: Andreas Engel, Center for Cellular Imaging and Nano Analytics, Biozentrum, University of Basel, Mattenstrasse 26, CH-4002 Basel, Switzerland. Tel.: +1 216 368 0411; fax: +1 216 368 1300.
** Correspondence to: Center for Molecular Protein Science, Department of Biochemistry and Structural Biology, Lund University, P.O. Box 124, SE-221 00 Lund, Sweden. Tel.: +46 46 2224195; fax: +46 46 2224116.
E-mail addresses: ahe13@case.edu (A. Engel), per.kjellbom@biochemistry.lu.se (P. Kjellbom).
[1] Present address: European Molecular Biology Laboratory, Meyerhofstrasse 1, 69117, Heidelberg, Germany.
[2] Present address: Department of Pharmacology, Case Western Reserve University, Cleveland, OH 44106, USA.

0005-2736/$ – see front matter © 2011 Elsevier B.V. All rights reserved.
doi:10.1016/j.bbamem.2011.12.006

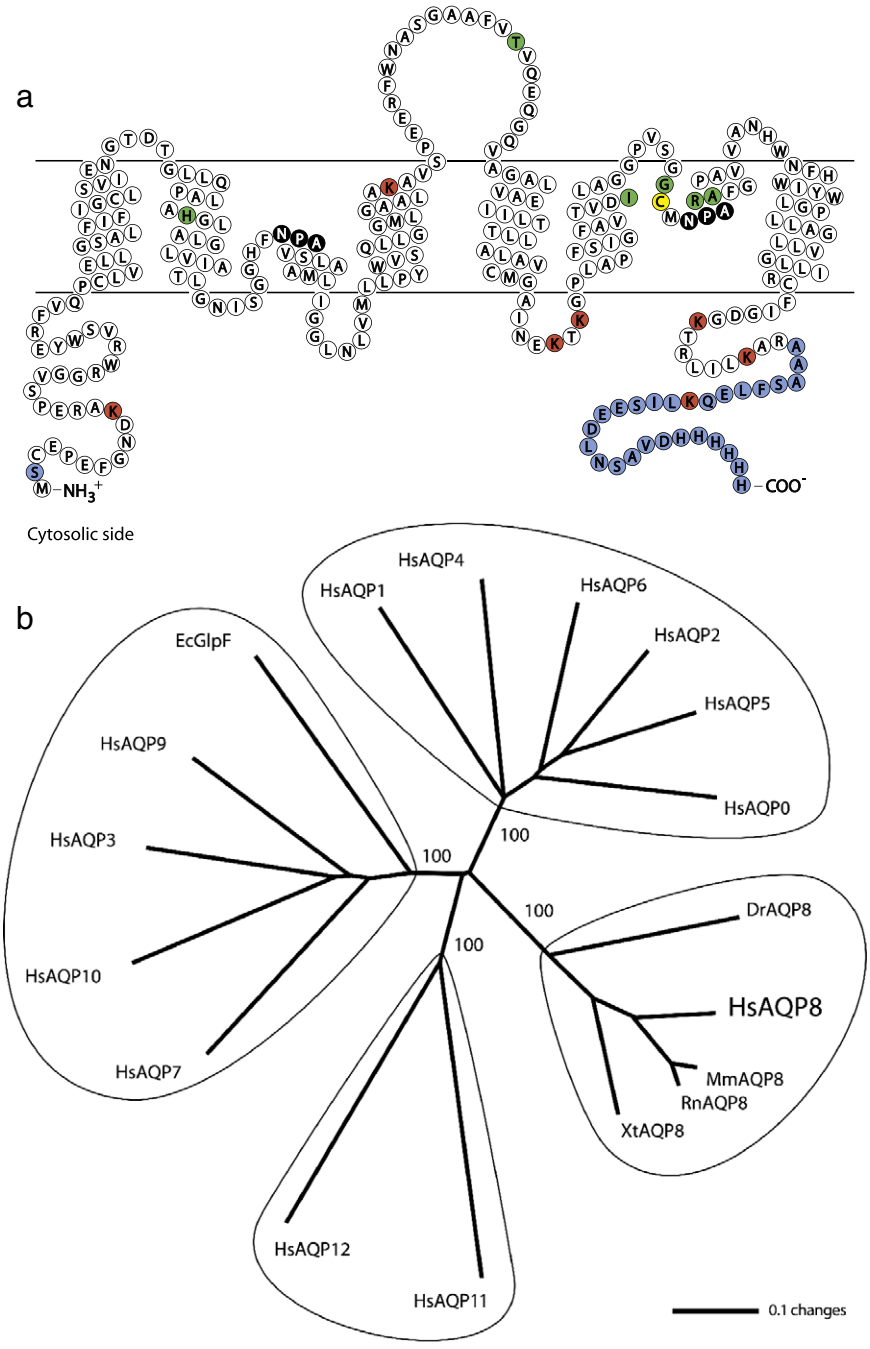

Fig. 1. Topology of HsAQP8 and phylogenetic analysis of all human aquaporins. (a) Schematic topology of HsAQP8 showing the 7 lysines in red, the conserved NPA-boxes in black, the conserved amino acids in the constriction region in green (from the N-terminal named H2, LC, H5, LE1, LE2 and LE3, see also Table 2), the cysteine responsible for mercury inhibition in yellow and the added amino acids in blue (S2 is included in *Pichia pastoris* start codon and the extension in the C-terminal constitutes a c-myc epitope and a His-tag). (b) Phylogenetic analysis of protein sequences of all the human (Hs) aquaporins and AQP8 protein sequences from additional species. The aquaglycerolfacilitator (EcGlpF) from *E. coli* was included as reference. Bootstrap values are shown only for the main branches, indicating 100% support for each subfamily when 1000 replicates were analyzed. Accession numbers: Dr, *Danio rerio*, NP_001004661.1; Mm, *Mus musculus*, NP_001102515.1; Rn, *Rattus norvegicus*, NP_062031.1; Xt, *Xenopus tropicalis*, NP_001107728.1.

[27] have been solved by X-ray and/or electron diffraction analysis. All these structures show the characteristic aquaporin topology and fold, first described for the human AQP1 [9] and the bacterial GlpF [10]. Most of the AQPs have been captured in their open conformation, but AQP0 [14], Aqy1 and SoPIP2;1 [22] have been found to exist in a closed conformation. To get further insights into the selectivity and transport mechanisms, it is of significant interest to resolve structures of representative aquaporin isoforms of each of the subfamilies. This would also improve our understanding of mutant phenotypes and facilitate the design of isoform-specific inhibitors.

Compared to the number of overexpressed and crystallized soluble proteins, only few membrane proteins have been overexpressed and structurally determined. A major hurdle is the production of functional membrane proteins for crystallization experiments. The overexpression problem is related to the capacity of the respective expression system and the properties of the membrane protein to be expressed. These factors are not fully understood and therefore often result in low yield and misfolding of the membrane protein [28,29]. Furthermore, to purify membrane proteins they need to be kept in solution by detergents whose properties influence the

stability of the protein [30], so the choice of detergent is crucial and needs to be optimized.

In comparison to other human AQPs, human AQP8 (HsAQP8) belong to a separate subfamily, which is distant from the water-specific aquaporins (AQP0, 1, 2, 4, 5 and 6), the aquaglyceroporins (AQP3, 7, 9 and 10) and the AQP11-12 subfamily. The substrate specificity of HsAQP8 has previously been addressed in several studies, using the *Xenopus* oocyte system [31,32] and by using yeast complementation studies [33], and HsAQP8 was in addition to water and hydrogen peroxide convincingly shown to be permeable to ammonia. In addition, purified rat AQP8 was reconstituted into planar lipid bilayers and found to be permeable to NH_3 but not to NH_4^+ [34]. Thus, the difference in the constriction region, also called the aromatic/arginine region, allows other solutes such as ammonia [33] and H_2O_2 [35] to permeate through HsAQP8 in addition to water, whereas neither urea nor glycerol can penetrate [36].

HsAQP8 is phylogenetically different from all other human AQP isoforms, possessing a unique constriction region resulting in a novel substrate specificity, and HsAQP8 is so far a relatively little studied aquaporin. HsAQP8 has been reported to be expressed in the kidney, in the gastrointestinal tract, in testis, airways and in the liver. Together with AQP6, but in contrast to the other eleven human AQP isoforms, HsAQP8 is localized to intracellular membranes and not to the plasma membrane [37]. The intracellular location of HsAQP8 has been reported to be the inner mitochondrial membrane [38,39], however, this localization has been questioned by other reports [40]. The biological relevance of a localization at the inner mitochondrial membrane has been suggested to be correlated with ammonia transport during the urea cycle [32] and the transport of reactive oxygen species in the form of hydrogen peroxide [35].

A structure of HsAQP8 is likely to deviate from the structures of the water-specific aquaporins, and would provide new information about aquaporin function and selectivity. Based on the number of expressed sequence tags (ESTs), HsAQP8 is expressed at a low level in native tissue. In pursuit of the goal to unravel the HsAQP8 structure, we show that it is possible to overexpress and purify a functional HsAQP8 using the methylotrophic yeast *P. pastoris* as host. Using different 2D crystallization methods and conditions, we obtained two-dimensional crystalline arrays differing in crystal form and quality. Highly ordered crystalline sheets diffracting to 3 Å were obtained by enzymatic cleavage of part of the N-terminal and the C-terminal region.

2. Material and methods

2.1. Amino acid sequence analyses

Alignment of the aquaporin protein sequences chosen for analysis was made in ClustalW [41], included in MacVector 8.0 (Oxford Molecular Ltd, U.K.), with manual adjustments to fit conserved motifs and avoid gaps in transmembrane helices [42]. The phylogenetic analysis of the unrooted Neighbor Joining tree was made in PAUP* 4.0 [43] where most of the variable N- and C-terminal regions were excluded. A schematic topology of human AQP8 (HsAQP8) highlighting the membrane regions (Fig. 1a) was created based on an alignment with human AQP1 (PDB ID: 1FQY).

2.2. Cloning and transformation

The EasySelect™*Pichia* Expression kit was purchased from Invitrogen. The human *aqp8* cDNA (I.M.A.G.E ID 5759105) was amplified with primers including 5′ *Eco*RI site and 3′ *Not*I site appropriate for cloning into the *P. pastoris* vector pPICZB. The forward primer used was CCCGAATT**CAAAATGTCT**TGTGAGCCTGAATTTGGC and the reverse primer AAGCGGCCGCCCGAGCCTTCAGGATGAGGC with restriction sites underlined and *P. pastoris* translational start site in bold. The *P. pastoris* start site was created by adding an extra serine directly after the start methionine and the native stop codon of human *aqp*8 was removed to add a c-myc epitope and 6× His-tag (HT) to the C-terminal, extending the expressed protein by 28 amino acids in total. The correct insertion of the construct into pPICZB was confirmed by sequencing. Prior to transformation into *P. pastoris* wild type strain X-33, the engineered plasmid was linearized by *Bst*XI and transformation was done by electroporation. As a negative control, empty pPICZB was linearized and used to transform strain X-33 in the same manner.

2.3. Screening for high expressing clones and scale-up

Small cultures were screened for high expression. Briefly, cell pellets from different times of methanol induction were disrupted by vortexing with glass beads and total cell lysate was analyzed by immunoblotting. A clone expressing the spinach aquaporin SoPIP2;1 was used as reference [44]. One transformant was chosen for large scale culturing in buffered glycerol complex medium and buffered methanol complex medium according to Karlsson et al. [44]. Methanol (0.5% final concentration) was added every 24 h to retain induction and cells were harvested by centrifugation after 48–144 h of induction and stored at −80 °C.

2.4. Membrane preparation from P. pastoris

30–35 g of cells were thawed and resuspended in 150 mL precooled breaking buffer (50 mM sodium phosphate buffer pH 7.4, 1 mM EDTA, 5% glycerol and 1 mM PMSF). Cells were disrupted in cold room using a 350 mL BeadBeater™ (BioSpec Products, Bartlesville, USA) containing 200 mL of glass beads (0.5 mm∅) and equipped with an ice-water cooling jacket by pulsing 12×30 s with intervening 30 s pauses. Cell debris was pelleted at 1400×*g* for 2×30 min at 4 °C with an additional breaking buffer resuspension step to get full recovery of membranes. Total membrane fraction was collected by ultracentrifugation of the supernatant at 150,000×*g* for 2 h at 4 °C. The membrane pellet was resuspended in precooled buffer A pH 7.8 (20 mM HEPES–NaOH, 50 mM NaCl, 10% glycerol and 2 mM β-mercaptoethanol) using a Potter–Elvehjem tissue grinder. For monitoring total membrane protein yield at different times of induction, cells were disrupted by three passages through a French Press at 16,000 psi and cell debris was removed and membrane was recovered by centrifugation.

2.5. Electrophoresis and immunoblotting

Proteins were separated according to Laemmli [45] with minor modifications. Samples solubilized for 1 h at room temperature in standard Laemmli solubilization buffer were separated on a 5% stacking gel and 12% separating gel. After electrophoresis, gels were either stained by Coomassie brilliant blue R-250 or transferred to a polyvinylidene diflouride membrane at 100 V for 1 h. HsAQP8 were detected by tetra-His antibody (Qiagen) diluted 1:2000 in Tris buffer saline and 3% bovine serum albumin. Anti-mouse IgG conjugated to horseradish peroxidase (GE Healthcare) was used as secondary antibody and the immunoblots were developed with ECL (GE Healthcare).

2.6. Detergent screen, protein solubilization and HsAQP8 purification

Small aliquots of the total membrane fraction were diluted with buffer B (20 mM HEPES–NaOH, 300 mM NaCl, 10% glycerol and 2 mM β-mercaptoethanol) and solubilized with different detergents added dropwise to a final total membrane protein concentration of 12 mg/mL and final detergent concentrations of 2% n-dodecyl-β-D-maltopyranoside (DDM), 2% n-decyl-β-D-maltopyranoside (DM), 2% n-dodecylphosphocholine (Fos-choline-12), 2% Cymal-6, 2% lauryldimethylamine-N-oxide (LDAO), 4% 3[(3-cholamidopropyl)dimethyl-ammonio]propanesulfonic acid (CHAPS), 2% n-undecyl-β-D-maltopyranoside (UDM), 4% n-nonyl-β-D-glucoside (NG); (all from

Anatrace) and 4% octyl-polyoligooxyethylene (Octyl-POE); (Alexis Corporation), respectively. Membranes were solubilized for 1 h at room temperature with gentle stirring. Unsolubilized membranes were collected by ultracentrifugation at 150,000×*g* for 30 min at 4 °C. Solubilization efficiency was analyzed by immunoblotting using the low critical micelle concentration (CMC) detergent DDM as efficiency control. Three detergent candidates DM, Cymal-6 and Fos-choline-12, were chosen for testing their effect on purification efficiency and protein stability. To ensure equal start condition, the total membrane fraction was solubilized with 2% DDM. The solubilized membrane protein fraction with a final concentration of 10 mM imidazole was divided into four equal aliquots and were mixed with Ni-NTA agarose (Qiagen) preequilibrated with buffer B and different detergents (0.4% DM, 0.04% DDM, 0.15% Cymal-6 and 0.3% Fos-choline-12) and incubated overnight at 4 °C with agitation. The mixtures were filled into empty PolyPrep columns (BioRad), the columns were washed with 40 bed volumes of buffer B with detergent and 70 mM imidazole, and HsAQP8 was eluted in buffer B with detergent and 300 mM imidazole. To check protein stability, the elutions were split and kept at 4 °C and at room temperature for 2 days. Samples were ultracentrifuged at 150,000×*g* at 4 °C for 40 min to pellet any precipitated protein and supernatants were analyzed by SDS-PAGE. Total membrane protein concentration was determined according to Bearden [46] and purified HsAQP8 concentration was determined by A_{280} where a calculated extinction coefficient of 42,970 M^{-1} cm^{-1} and a molecular weight of 29,934.9 Da were used [47,48].

2.7. Large-scale membrane protein solubilization and HsAQP8 purification

DM was chosen for large-scale solubilization and purification, which was carried out as above but the final concentration of DM for solubilization was 3%. Routinely, 250–300 mg of total membrane protein were solubilized and mixed with 1 mL of Ni-NTA agarose.

2.8. Reconstitution and stopped flow analysis

Different detergent and lipid combinations were screened for optimal vesicle formation verified by negative stain electron microscopy (EM). Purified HsAQP8 was mixed with detergent and lipid to the final concentrations of 2 mg/mL of lipid (3:7 POPS/POPC (1-palmitoyl-2-oleoyl-*sn*-glycero-3-phosphoserine/1-palmitoyl-2-oleoyl-*sn*-glycero-3-phosphocholine, Avanti Polar Lipids)), 2% DM and with the LPRs adjusted to 10, 30, 60 and 90 (w/w). The mixture was dialyzed against 20 mM Tris–HCl, pH 8.0, 150 mM NaCl and 0.03% NaN_3 with a molecular cut-off of 12–14 kDa for 7 days at room temperature. The proteoliposomes were passed once through a 0.2 μm filter. Size homogeneity was checked by negative stain EM prior to stopped flow analysis. Control liposomes were made in parallel without protein. The proteoliposomes and control vesicles were subjected to an inwardly directed osmotic gradient generated by rapid mixing of one volume 200 mM sucrose and one volume of proteoliposomes in a stopped flow instrument. A 530 nm beam was used for monitoring the proteoliposomes size change. The increase in scattered light, due to the decrease of vesicle volume, was monitored at 90° angle during 0–3 s at room temperature. Water channel activity was blocked by preincubating the LPR 10 proteoliposomes in 2 mM $HgCl_2$ for 1 h at room temperature. Traces of 5–10 individual runs per experiment were normalized, averaged and fitted to a single exponential equation $y = y_0 - Ae^{-kx}$, where k is the first order rate constant.

2.9. Two-dimensional crystallization and Lys-C treatment

Purified HsAQP8 at a concentration of 1 mg/mL was mixed with different lipids solubilized in 2% DM to achieve final LPRs. After 1 h preincubation at room temperature, 60 μL aliquots were dialyzed against detergent-free buffers using a molecular cut-off of 10 kDa. After 12, 24 or 36 h at room temperature samples were moved to 37 °C for 48 h and thereafter back to room temperature for 2 days. Subsequently, the best crystallization procedure was repeated and tuned in the temperature-controlled dialysis machine [49]. The following temperature profile was selected: 12 h at 20 °C, 12 h linear increase to 37 °C, 48 h at 37 °C, 24 h linear decline to 20 °C. To each 100 μL sample a total of 1 μg of Lys-C was added after 36 h of the crystallization procedure. Lys-C is a protease that specifically cleaves peptide bonds C-terminally at Lys, at pH 7.0–9.0. The summary of 2D-crystallization experiments is given in Table 1.

2.10. Electron microscopy

Negative stain EM was used to verify sample homogeneity of single particles and to screen crystallization trials. Four μL of purified protein solution (0.1–0.001 mg protein/mL) or 4 μL of crystal sample were adsorbed for 5 s or 1 min, respectively, to carbon-coated copper grids previously rendered hydrophilic by glow discharging. Grids were washed with 4 drops of nanopure water and stained twice for 12 s with 5 μL of 2% uranyl acetate. Negatively stained single particles and crystal specimens were imaged with a transmission electron microscope Phillips CM-100 operated at 80 kV and 100 kV, respectively. Electron micrographs of crystal specimens were taken at magnifications of 7000× to 52,000× and recorded on Kodak SO163 film. Specimens of highly ordered 2D crystals were further analyzed by cryo electron microscopy. Selected samples were embedded in 7% trehalose on molybdenum grids, covered with a carbon film that was previously evaporated on mica and floated on the grid [50]. Electron micrographs were taken on Kodak SO163 film at low dose (<10 electrons per $Å^2$) at magnification of 50,000× with a Phillips CM-200 FEG microscope operated at 200 kV. The diffraction patterns were recorded with a Gatan UltraScan™ 1000 2 k×2 k slow scan CCD camera at −175 °C.

2.11. Image processing

Electron micrographs of negatively stained HsAQP8 tetramers were scanned at a resolution of 4 Å/pixel, single particles were selected by eye using the BOXER program and processed using EMAN [51].

Table 1
Summary of 2D-crystallization experiments.

Parameter	Range tested	Optimal condition
Detergent	DM, DDM, Cymal-6, Foscholine-12	DM
Lipids	E. coli, E.coli polar, soy, liver, brain, DMPC, DOPS, DOPE, DOPC, DOPA, POPS, POPC, POPE, POPA, POPE:POPC (1:1, 3:7), POPS:POPC (3:7), POPA:POPE:POPC (1:2:7), POPA:POPC (1:1, 3:7), DOPE:DOPC (3:7), DOPS:DOPC (3:7), DOPA:DOPC (1:1, 3:7), DOPA:DOPE:DOPC (1:2:7)	POPE:POPC (3:7)
LPR	0.1–1.3	0.25–0.30
Protein concentration	0.5–2 mg/mL	1 mg/mL
pH	4.0–9.0	7.0
Buffer	Citrate, MES, Hepes, Tris, Bicine	Hepes
NaCl	50 mM–1 M	100 mM
$MgCl_2$	0–20 mM	–
$CaCl_2$	0–20 mM	–
EDTA	0–5 mM	5 mM
DTT	0–10 mM	2 mM
Glycerol	0–20%	10%
Temperature/ temp change	4 °C, 20 °C, 37 °C, 20 °C→4 °C→20 °C, 20 °C→37 °C→20 °C, 37 °C→20 °C	20 °C→37 °C→20 °C

Electron micrographs of trehalose embedded 2D crystals taken at 50,000× magnification at low dose and at liquid nitrogen temperature, were scanned using a Heidelberg Primescan D7100 scanner at a step size of 5 μm resulting in a resolution of 1 Å/pixel. Digitized images were analyzed and processed either with the 2dx- or the IPLT image processing software [52,53]. Crystalline single layers from undigested HsAQP8 samples and double layer LysC digested crystals were processed identically - either following the MRC procedure (2dx) or calculating correlation averages (IPLT). For the latter, the lattice was indexed and the CTF was corrected. All subsequent processing steps were executed on the CTF corrected image. These included calculation of the Fourier filtered image, selection of a reference patch, calculation of the cross-correlation function and peak-search to identify unit cell positions. Peak positions were refined to sub-pixel accuracy by fitting Gaussians to the peaks. Intermediate correlation averages obtained served as reference to refine the averaging process until no further change was observed. Correlation averages obtained were p4 symmetrized. The packing arrangement of these crystals was verified by assembling a model from the tetramers of the undigested crystal.

3. Results

3.1. Phylogenetic analysis and the variation of amino acids in the constriction region

To visualize the protein sequence variation between the different isoforms of the human AQPs and the similarities of AQP8 sequences from different species, a phylogenetic tree was constructed (Fig. 1b). The analysis confirmed that AQP8 from divergent vertebrates form a monophyletic clade [54]. Bootstrap values calculated based on 1000 replicates indicate 100% support for the 4 subfamilies. The constriction region of the selectivity filter of HsAQP8 deviates significantly compared to the other human AQPs but is identical to other mammalian AQP8s and shows high similarity to the *Arabidopsis thaliana* tonoplast intrinsic proteins (AtTIPs) as seen in Table 2. The variation among human aquaporins is reflected in the phylogenetic tree, where the AQPs divide into the different subfamilies in accordance to differences in the amino acids in the ar/R region. The structure and the topology of aquaporins are remarkably conserved (Fig. 1a), however, the primary sequence of HsAQP8 is quite distant from the primary sequence of all other human AQP isoforms. Based on an alignment (Supplemental material Fig. 1) the sequence identity between HsAQP8 and HsAQP1 is only 28%. HsAQP1 belongs to the canonical water-specific clade (represented by HsAQP0, 1, 2, 4, 5, and 6). An alignment of all human AQPs plus some additional AQPs can be found in the Supplemental material (Fig. 2).

Table 2
Amino acids of the constriction region. Conserved amino acids in the alignment of the constriction region (H2, H5, LE1 and LE2) and two structurally adjacent amino acid positions (LC and LE3) of human AQPs and two selected plant AQP subfamilies (see also Fig. 1a). The numbers in superscript refers to the amino acid of HsAQP1 and amino acids in brackets are only present in one member of that subfamily. H2 and H5 refer to helix 2 and 5, respectively, and LC and LE refer to loops C and E, respectively. HsAQP0, 1, 2, 4, 5 and 6 constitute the water-specific aquaporin subfamily and HsAQP3, 7, 9 and 10 constitute the aquaglyceroporin subfamily.

Isoform	H2	LC	H5	LE1	LE2	LE3
HsAQP0,1,2,4,5,6	F^{56}	N^{127}(T)	H^{180}	C^{189}/A	R^{195}	S^{196}
HsAQP8	H	T	I	G	R	A
HsAQP11,12	L	P/S	V/A	A	L	A
HsAQP3,7	F	T	G	Y	R	D
HsAQP9	F	T	A	C	R	D
HsAQP10	G	T	G	I	R	D
Plant PIPs	F	N	H	T	R	S
AtTIPs	H(N)	F/H(Y)	I(V)	A/G	R/V(C)	S/A

3.2. Cell yield and membrane recovery

One clone expressing high levels of HsAQP8 showed a cell wet weight increase by around 45% when inducing for 144 h vs. 48 h while the total membrane recovery determined by weight increased by 75%. Comparing methanol induction for 144 h vs. 120 h did neither increase the cell amount nor the amount of total membrane but increased the total membrane protein content by more than 100%. Routinely, 1 L of culture gave 32–34 g of cells harvested 144 h after induction. After breaking the cells, 7–8 g of total membrane fraction was collected giving around 0.25 g of total membranes per gram cells. 10% of the total membrane fraction constituted total membrane protein, i.e. 1 L of culture gave around 800 mg membrane proteins or 24 mg membrane protein per gram cells.

3.3. Detergent screen and protein stability

To be able to remove the detergent in later steps, detergents with relatively high CMC were screened. DDM, a low CMC detergent able to solubilize HsAQP8 with a satisfying yield, was used as reference. DM, Fos-choline-12 and Cymal-6 showed equal solubilization efficiency as the reference and were subsequently used in the purification and stability tests (Fig. 2a). LDAO, CHAPS, UDM, NG and Octyl-POE were less efficient in solubilizing HsAQP8. Protein purified by DM and Cymal-6 showed the best yield after Ni-NTA affinity purification of the His-tagged HsAQP8. Using DM resulted in 90% yield, Cymal-6 in 80% yield, and Fos-choline-12 in 30% yield. Prior to the elution step, it seems that Fos-choline-12 causes a partial release of the protein from the Ni-NTA agarose resulting in HsAQP8 being present in the first twenty 1 mL wash fractions (Fig. 2b). This was not observed with the other detergents. The purified protein fractions showed neither precipitation nor degradation irrespective of detergent and temperature tested.

3.4. Membrane protein solubilization and HsAQP8 purification

DM was chosen for large-scale solubilization and HsAQP8 was purified using Ni-NTA agarose. Two mg of pure HsAQP8 was obtained from 1 L of culture, i.e. 0.06 mg pure HsAQP8 per gram of cells.

3.5. Single particles and sample homogeneity

Sample homogeneity and monodispersity were checked by negative stain EM of single particles. As displayed in Fig. 2c the purified HsAQP8 preparation exhibits particles of uniform size, many having a central stain-filled depression. Micrographs taken at a magnification of 50,000× were digitized at 4 Å/pixel, and 490 particles showing a central cavity were picked and classified using the EMAN software [51]. The representative class average shown in Fig. 2c (inset) reveals the square shape and 4-fold symmetry of the HsAQP8 complex, which has a side length of about 7 nm.

3.6. Reconstitution and stopped-flow analysis

To measure the water channel activity by stopped-flow spectrophotometry, HsAQP8 was reconstituted into proteoliposomes. After dialysis, proteoliposome formation was analyzed by negative stain EM. Optimal conditions for liposome formation were obtained by using POPS/POPC (1-palmitoyl-2-oleoyl-*sn*-glycero-3-phosphoserine/1-palmitoyl-2-oleoyl-*sn*-glycero-3-phosphocholine) (3:7 w/w ratio) solubilized in DM. To test the functionality of the heterologously expressed HsAQP8, a ternary mixture of purified protein and POPS/POPC all solubilized in DM, was dialyzed in parallel with control liposomes containing no protein. Water transport was monitored by stopped-flow spectroscopy after exposing the proteoliposomes to a hyperosmotic shock causing an aquaporin-dependent shrinkage of the proteoliposomes and a change in light scattering (Fig. 2d).

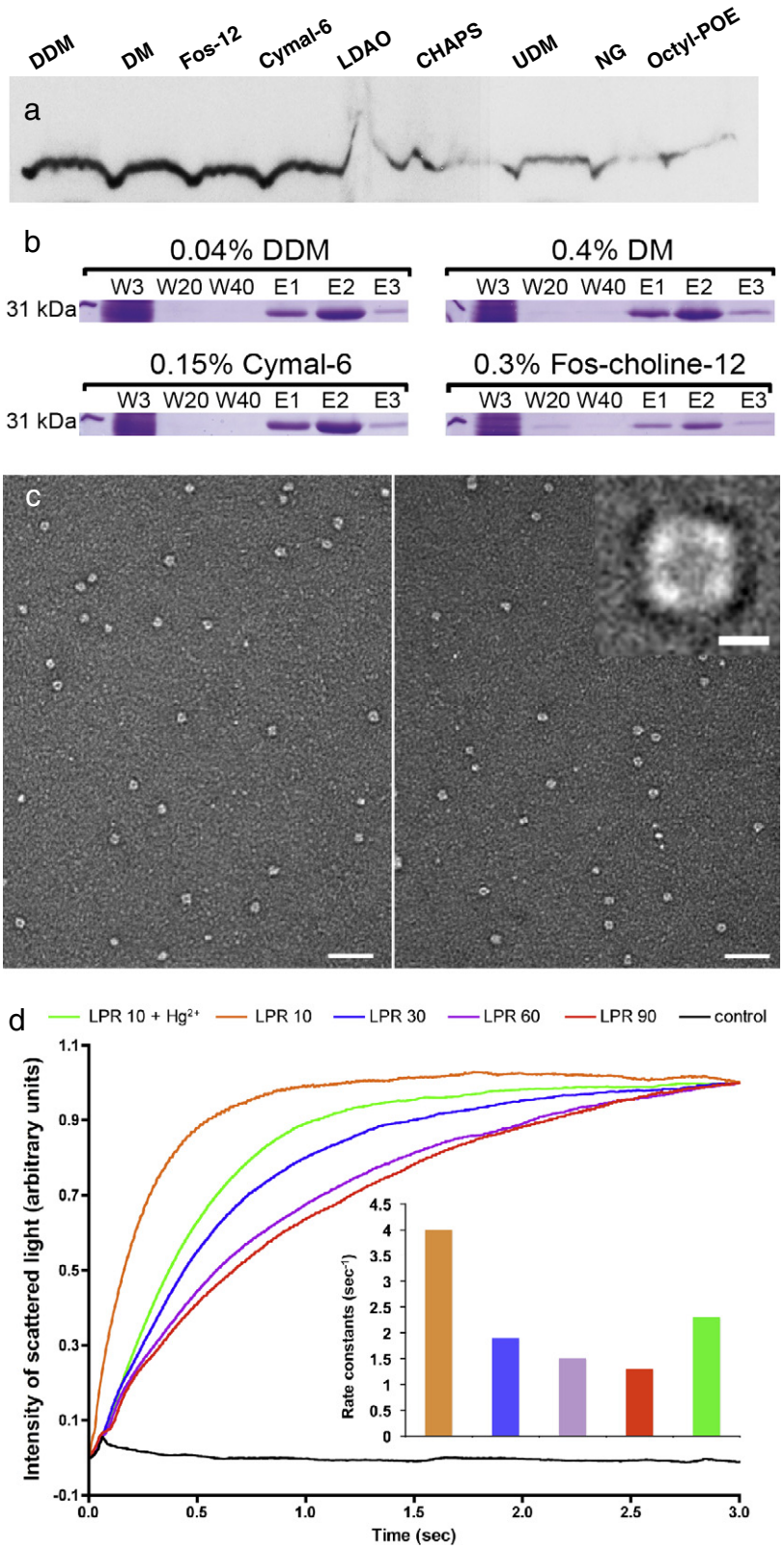

Fig. 2. Detergent screen, purification and functional analysis of HsAQP8. (a) Western blot showing different detergents solubilizing HsAQP8 detected by a tetra-His antibody. (b) SDS-PAGE showing test purification with the 3 best solubilizing detergents using DDM as control. Unspecifically bound proteins are washed off during the first few washing fractions (represented in lane W3). Only wash fractions W3, W20 and W40, and the first three 1 mL elutions, designated E1–E3, are shown on gels stained with Coomassie R-250. (c) Electron micrographs of negatively stained HsAQP8 preparations reveal monodisperse single particles after purification in DM (left) and in DDM (right). The inset on the right shows a class average calculated from 490 DDM-purified particles. Scale bars correspond to 20 nm in left and right panels and to 5 nm in the inset. (d) Stopped-flow analysis of HsAQP8 at different lipid-to-protein ratios (LPRs). Traces display a faster increase in scattered light when increasing the protein content of the proteoliposomes. Traces of 5–10 individual runs per experiment were normalized, averaged and fitted to single exponentials. The bar diagram shows the rate constants of the averaged single exponential fits for proteoliposomes at different LPRs including the blockage by Hg^{2+}.

Calculated rate constants are: 4.0 s^{-1} at LPR 10, 1.9 s^{-1} at LPR 30, 1.5 s^{-1} at LPR 60 and 1.3 s^{-1} at LPR 90. It is known that water transport in AQP8 is inhibited by mercury binding to a cysteine residue in the pore region [31]. Proteoliposomes at LPR 10 blocked with mercury had the rate constant of 2.3 s^{-1}, which could be expected if ~50% of the HsAQP8 were inserted in opposite orientation. Empty control liposomes did not show any significant change in the intensity of scattered light within 3 s after exposure to the osmotic gradient (Fig. 2d).

3.7. Two-dimensional crystallization of HsAQP8

To optimize HsAQP8 crystallization, a variety of conditions were tested: a range of LPRs, different lipids, detergents and buffers at various pH as well as different salts concentration. During the crystallization process the temperature profile had a significant influence on the formation, size and quality of the crystals. For instance, tubular crystals were formed when samples were moved to the higher temperature during the first 36 h of crystallization (Fig. 3a, b). In contrast, incubation at room temperature for the first 36 h and subsequent temperature increase yielded large amounts of regularly packed sheets and vesicle-like structures of a few micrometers in size. The quality of HsAQP8 2D crystals improved during a two-week-long storage at 4 °C. Most of the crystallization experiments were carried out in a temperature-controlled dialysis machine (see Section 2.9).

Solubilized and highly purified HsAQP8 was reproducibly reconstituted into lipid bilayers using a mixture of POPE (1-palmitoyl-2-oleoyl-*sn*-glycero-3-phosphoethanolamine) and POPC lipids in the ratio of 3:7 (w/w) (Fig. 3a–d). When the protein concentration was over 1 mg/mL in the crystallization mixture well-ordered 2D crystals were obtained under optimal 2D crystallization conditions (Table 1): POPE/POPC lipids (in ratio 3:7), LPR of 0.25–0.30 and the dialyzing buffer containing 20 mM HEPES–NaOH, pH 7.0, 100 mM NaCl, 5 mM EDTA, 2 mM DTT and 10% glycerol (Fig. 3d).

3.8. Lys-C treatment of 2D crystals

At the C-terminal of the protein the HsAQP8 construct contains a 10 amino acid c-myc epitope (EQKLISEEDL), a 6 amino acid His-tag and proper linkers (11 amino acids) (Fig. 1a). We suspected that this 27 amino acid long sequence might possibly disturb crystallization and therefore partly removed it enzymatically during the dialysis procedure. In the 283-amino acid long HsAQP8 construct 7 possible Lys-C cleavage sites can be identified (Fig. 1a). When the protein is

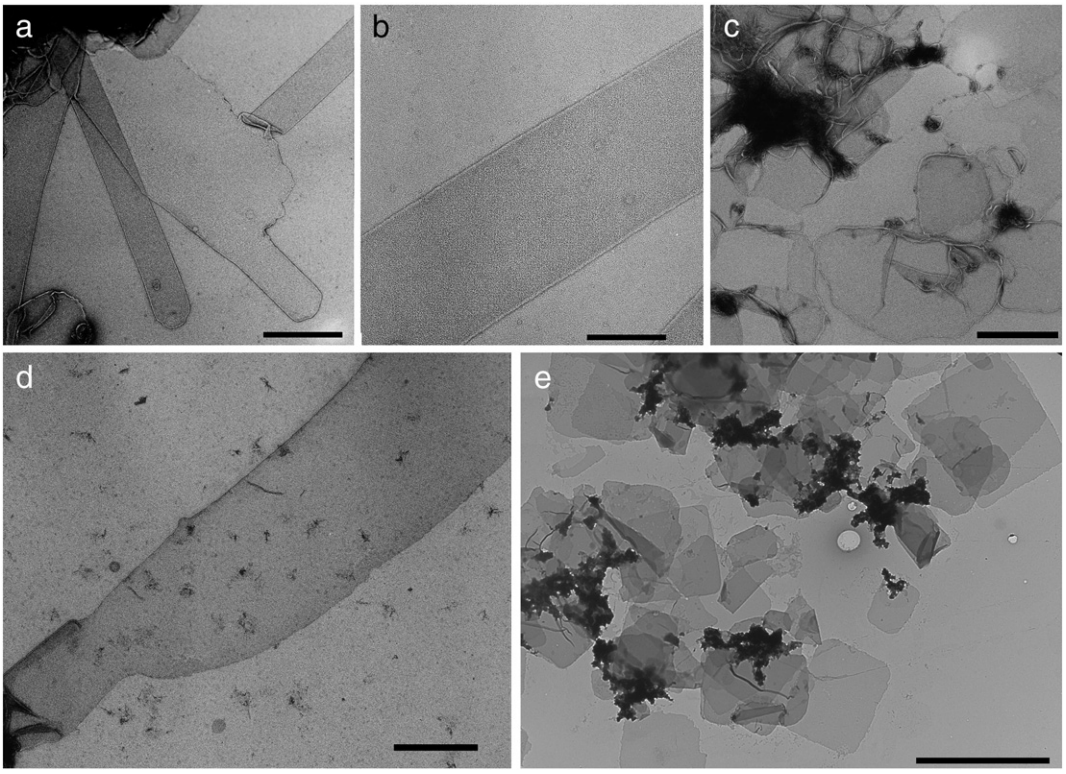

Fig. 3. Two-dimensional (2D) crystals of HsAQP8 reconstituted by dialysis in the presence of lipid. (a) Electron micrograph of negatively stained HsAQP8 2D crystals. Crystals appear as ordered tubes with a diameter of about 360 nm and a length of several micrometers, often attached to aggregates, vesicles or unrolled/open tubes. Scale bar corresponds to 800 nm. (b) A crystalline HsAQP8 tube recorded at a magnification of 50,000×. Scale bar corresponds to 200 nm. (c) When 5 mM EDTA is added to the reconstitution buffer, large vesicles and sheets of regularly packed HsAQP8 emerge. Scale bar corresponds to 1 μm. (d) Overview of a large HsAQP8 2D crystal obtained under the optimized conditions. Such crystals are large double-layered mono-crystalline protein–lipid arrays. Scale bar corresponds to 1 μm. (e) Electron micrograph of negatively stained Lys-C treated 2D double-layered HsAQP8 crystals exhibiting diameters of several micrometers. Scale bar corresponds to 5 μm. (f) Correlation average calculated from a trehalose embedded crystal produced under the optimized conditions that was recorded at 200 kV, low dose and liquid nitrogen temperature. The map shows 2×2 unit cells having a side length of 72 Å. Areas between bright protein tetramers represent the lipid bilayer and the asterisk marks the putative location of the C-erminus. (g) A model of the packing arrangement of the Lys-C treated HsAQP8 crystal was assembled from tetramers displayed in (f). Scale bar is 100 Å. (h) Correlation average of a Lys-C treated HsAQP8 2D crystal. The map displays 2×2 unit cells having a side length of 136 Å. Four distinctly delineated tetramers are visible. (i) A region of the Fourier filtered micrograph yielding the correlation average (h) reveals the packing arrangement of HsAQP8 tetramers and the lattice disorder. Distinct tetramers (marked with +) form 'cornerstones' of the lattice with tetramers in between assuming different positions, as marked with up/down arrows. (j) IQ plot [66] of the image from which the correlation average shown in (f) was calculated. After two rounds of unbending, reflections having an IQ value ≤4 extend out to a resolution of 8 Å. Ellipses show the zero crossings of the contrast transfer function. The edge of the plot is at a resolution of 7 Å in horizontal or vertical direction. (k) Electron diffraction pattern of a frozen-hydrated Lys-C treated HsAQP8 2D crystal. Sharp diffraction orders marked in the inset correspond to a resolution of 3 Å (arrow) and 3.3 Å (arrowhead). The lattice disorder manifests itself by smears extending along the lattice lines over three diffraction orders in a systematic manner (one example marked with an asterisk).

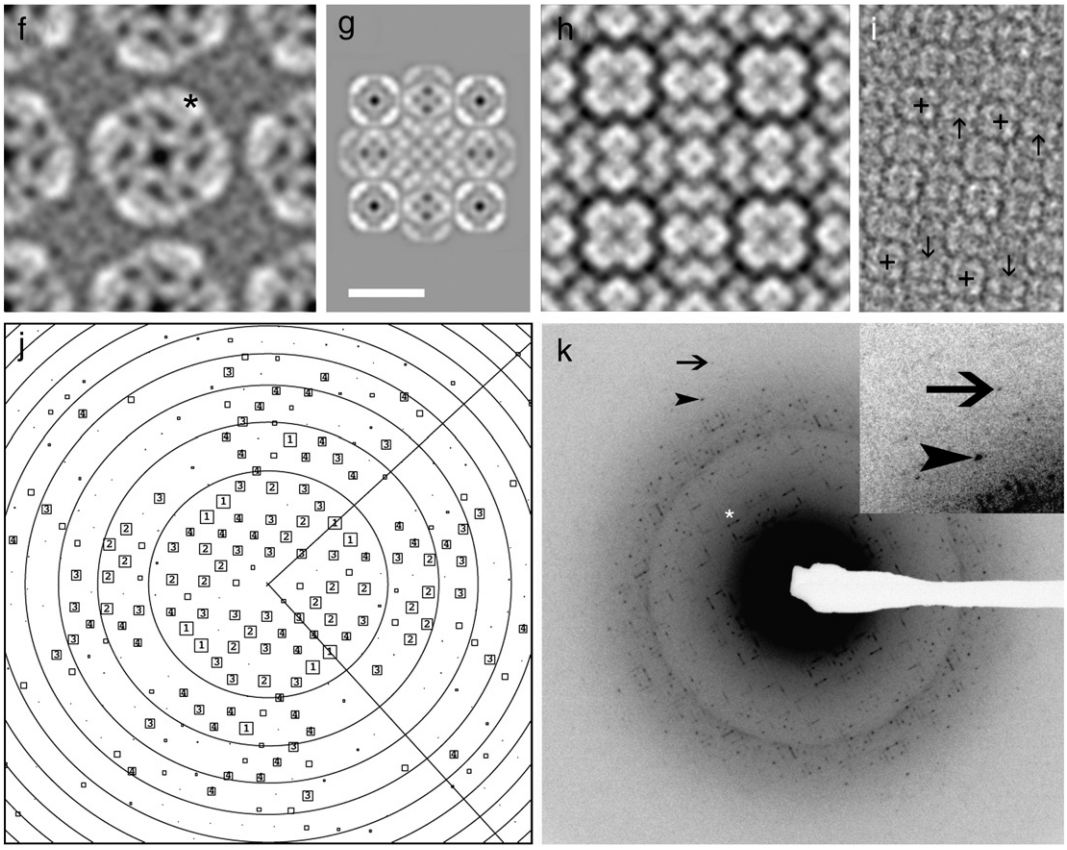

Fig. 3. (*continued*).

embedded in a lipid bilayer, 6 of these Lys are likely to be exposed to the enzyme. One Lys is positioned in the N-terminal region, two Lys in the cytosolic D-loop and three Lys in the C-terminal region of HsAQP8. SDS-PAGE analysis performed after the addition of the enzyme showed ~80% removal of at least the 18 amino acids in the C-terminal including the His-tag. In ~20% of the protein only a peptide corresponding to the 11 amino acids from the N-terminal is lost (Fig. 4). Importantly, the Lys-C treatment resulted in large rectangular protein–lipid arrays (Fig. 3e) that exhibited an electron diffraction pattern corresponding to a resolution of 3 Å (Fig. 3k).

3.9. Projection maps of the undigested and digested forms of HsAQP8 crystals

A large variety of crystals, grown at different 2D crystallization conditions, resulted in diverse protein packing arrangements in reconstituted lipid bilayers and a number of 2D crystal lattice parameters. EM of negatively stained reconstituted samples revealed well-ordered 2D crystalline sheets with a diameter of 2 μm and a length of several micrometers (Fig. 3d). Lattice vectors of sheets grown in buffer containing 100 mM or 1 M NaCl were $a = b = 72$ Å, $\gamma = 90°$. The correlation average [55] calculated from such a crystal embedded in 7% trehalose, recorded at low dose and at liquid nitrogen temperature, exhibits an aquaporin-like morphology with one tetramer per unit cell (Fig. 3f). Tetramers exhibited four prominent domains at their periphery that are likely to represent the 27 amino acid long C- and the 11 amino acid long N-termini. These domains appear to form the protein–protein interfaces leaving empty lipid regions between the tetramers. After unbending this crystal using the 2dx software [56], diffraction orders out to 8 Å resolution were detected (Fig. 3j). Unfortunately, ordered regions of these 2D crystals were too small for yielding electron diffraction to high resolution. Another crystalline form had lattice parameters $a = 68.5$ Å, $b = 133$ Å, $\gamma = 100°$ with a unit cell housing two tetramers in an up-and-down orientation, as judged from the different staining of the two tetramers. However, the crystalline order was poor (data not shown).

Addition of Lys-C protease during the crystallization process induced a significant change in the packing arrangement that resulted in lattice parameters $a = b = 136$ Å, $\gamma = 90°$ (Fig. 3g–i). Lys-C treated HsAQP8 2D crystals were embedded in 7% trehalose and low-dose images and diffraction patterns were collected at liquid nitrogen temperature and 200 kV. Diffraction patterns of digested crystals recorded with a CCD camera showed sharp spots out to 3 Å resolution. The two orders marked by a black arrow and an arrowhead in Fig. 3k corresponds to a resolution of 3 Å and 3.3 Å, respectively. However, not only sharp spots but also lines along lattice lines reaching over 3 diffraction orders are visible in such diffraction patterns (Fig. 3k, asterisk). These lines exhibited a systematic pattern with p4 symmetry, and they appear to be related to the packing arrangement of AQP8 tetramers. Inspection of regions of the Fourier filtered image of one 2D crystal treated by Lys-C shows lines of tetramers arranged in doublets. One of them (marked with '+' in Fig. 3i) is always more distinct than the other, which can be shifted either upwards (↑) in some rows, or downwards (↓) in others. Often the second tetramer is not clearly visible at all. The correlation average displayed in Fig. 3 h exhibits distinct, clearly delineated tetramers that lack the vorticity of the AQP8 tetramer from a single layer. In contrast, the map does not reveal clear tetramers in between those 'cornerstones', but a structure resembling overlapping tetramers. Measurements with the atomic force microscope showed the crystals to be double layered (data not shown), which was corroborated by occasional breaks of the crystals at their periphery, where two layers could be discerned. Hence, we produced two possible packing arrangement models from the AQP8 tetramer map shown in Fig. 3f, both assembled from two layers in opposite orientation. In one model the second tetramer of the pair had the same handedness, i.e.

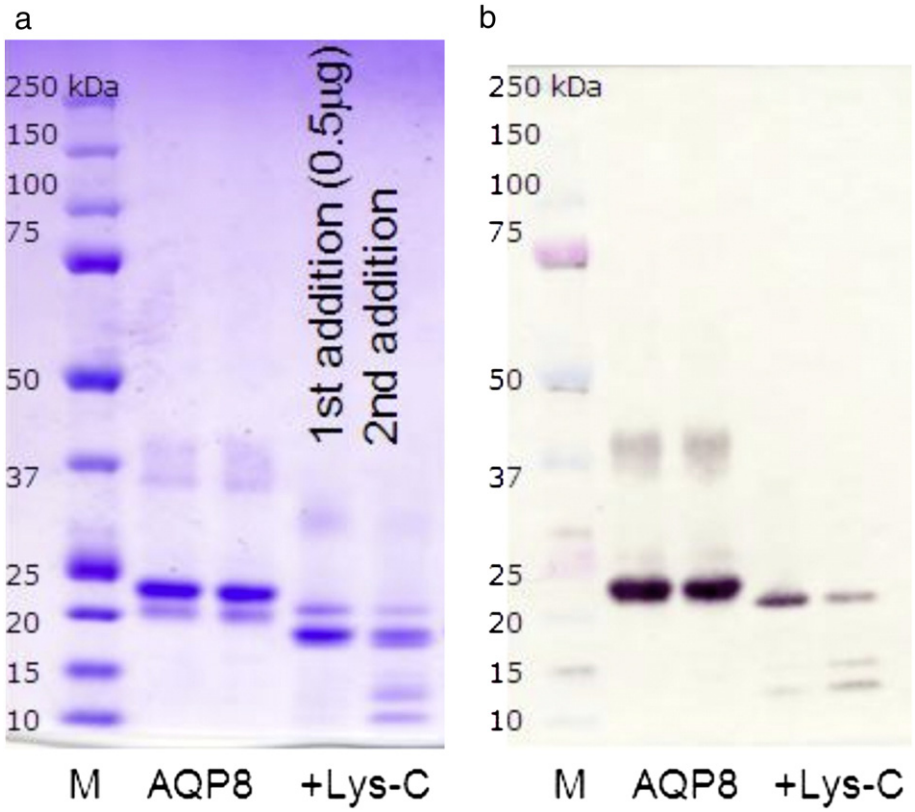

Fig. 4. (a) Coomassie stained SDS-PAGE gel and (b) immunoblot of untreated and Lys-C treated HsAQP8 probed by a tetra-His antibody. After addition of Lys-C 100% of the protein is affected since no band of the same size as the untreated protein is seen on the Coomassie stained gel. In ~20% of the HsAQP8 a peptide of around 1 kDa is lost corresponding to the 11 amino acids at the N-terminal (Fig. 1a). This cleaved protein has still an intact His-tag as detected by the antibody; upper band in (a) lanes 4 and 5 and its corresponding band in (b) lanes 4 and 5. In ~80% of the HsAQP8, the Lys-C treated protein has lost a C-terminal peptide of 18 or 29 amino acids cleaved downstream of K265 or more probably K254 (Fig. 1a) giving a protein without a His-tag. The lower faint band of untreated HsAQP8 on the Coomassie stained gel is suspected to be unspecific degradation of the C-terminal.

the same orientation in the membrane as the first, whereas in the other model its orientation was opposite. The projection of the first model is displayed in Fig. 3g. The cross correlation of this model with the map in Fig. 3h had a value of 0.313, whereas the one of the second model was 0.233. Therefore, we conclude that tetramers in one layer are all oriented in the same direction with respect to the membrane plane.

4. Discussion

4.1. Analysis of aquaporin primary sequences and the variations in the constriction region

It is established that AQP8 differs in solute specificity as compared to water-specific aquaporins [33,35,36]. Aligning aquaporin primary sequences where conserved motifs were fitted and gaps avoided in the transmembrane regions, a phylogenetic tree was constructed (Fig. 1b). This analysis confirmed the distinct clustering of the sequences of the AQP8 subfamily where the orthologs from different species create a separate monophyletic clade (Fig. 1b). The identification of AQP8 orthologs in bone fish indicate that this subfamily was formed more than 450 million years ago [57]. By comparing the crucial amino acids in the constriction region of the selectivity filter, major differences between AQP8 and the other aquaporin subfamilies were seen (Table 2). Taken together, the constriction region of HsAQP8 is highly similar to AtTIPs and when comparing e.g. wheat (*Triticum aestivum*) TIP2;1 (TaTIP2;1) and HsAQP8 they are identical. By homology modeling of the wheat TaTIP2;1, using the bovine AQP1 structure, widening of the pore region is seen as compared to AQP1 [33]. That model suggests that larger molecules are able to penetrate the pore. It has been shown that mutating the TaTIP2;1 constriction region, in order to mimic the corresponding region in bovine AQP1, abolished the ammonia transport but did not affect the water permeability of mutated TaTIP2;1 [32,33]. Due to the identical constriction regions of HsAQP8 and TaTIP2;1 these results could be valid for HsAQP8.

4.2. Expression of HsAQP8

In order to obtain high-resolution protein structures large amounts of functional purified protein is needed. It has been shown that many proteins have certain preferences regarding the lipid content of the host for expression [58], which makes the host selection critical. Also the codon usage preference in the organism could be a limiting factor in heterologous expression and, in some cases, it is worth to optimize the gene prior to cloning [59]. In order to obtain high levels of HsAQP8 protein the induction time had to be optimized. Interestingly, from 120 h, the cell wet weight and total membrane recovery did not increase but the total membrane protein content doubled. Prolonging the induction time seems to allow the cells to invest more into membrane protein expression rather than producing new membranes.

4.3. Membrane recovery, membrane protein solubilization and HsAQP8 purification

In previous work, urea and alkali treatment of the total membrane fraction have greatly enriched the AQPs prior to solubilization and purification [60,61]. This pretreatment has been successfully used both for the purification of AQPs from native tissue [60,62] and heterologously expressed AQPs [20,44]. However, for HsAQP8 the urea and

alkali treatment resulted in a very low yield of purified protein. HsAQP8 was instead directly solubilized from the total membrane fraction. After solubilization and binding of the protein to Ni-NTA beads a thorough washing step with a high imidazole concentration was introduced to eliminate contaminating endogenous *P. pastoris* membrane proteins.

4.4. Detergent screen and protein stability

To avoid a protein stability problem in the crystallization trials, a wide detergent screen was performed. Detergents with different structural properties were chosen. Since initial experiments using DDM had shown efficient solubilization DDM was used as a control, however, for efficient detergent removal by dialysis the CMC of DDM is too low. As expected, DM showed solubilization efficiency comparably to DDM since these detergents are related and share properties (Fig. 2a). On the other hand, Fos-choline-12 solubilized HsAQP8 sufficiently well but caused a considerable loss of protein in the washing step (Fig. 2b). We assume that this is an effect of the detergent's phosphate group competing for binding to the resin alternatively causing a release of Ni^{2+} from the resin. Recently, another group reported the expression, purification and functional analysis of human AQP8 [31]. They used *Saccharomyces cerevisiae* as a host for expression and the detergent octyl-β-D-glucopyranoside (OG) for the solubilization, however, the yield of AQP8 was not reported. When we solubilized and purified HsAQP8 with OG, a thin cloud was apparent in the purified fraction at a protein concentration of around 0.8 mg/mL suggesting protein aggregation.

4.5. Single particle and sample homogeneity

Single particle electron microscopy was used to assess the quality of HsAQP8 particles purified in DM and DDM, and their suitability for 2D crystallization trials. Electron micrographs of negatively stained HsAQP8 proved the monodispersity and homogeneity of samples. The lack of aggregates indicated that HsAQP8 was stable (Fig. 2c). To ascertain the tetrameric nature of the particles, 490 views exhibiting a central, stain-filled depression were selected and classified in EMAN [51]. A representative class average reveals a square shaped particle with a side length of about 7 nm (Fig. 2c, inset). This single particles analysis corroborates the 4-fold symmetry of the purified HsAQP8, which is typical for all known aquaporins.

4.6. Reconstitution and stopped-flow analysis

Different combinations of detergents and lipids were screened for vesicle formation and verified by negative stain EM. *E. coli* polar lipids in combination with e.g. OTG and OG have been used before for stopped-flow analysis [31,44]. In our experiments, *E. coli* polar lipids solubilized with DM did not form vesicles even after a long time of dialysis. However, POPS/POPC solubilized in DM formed spherical vesicles within one week of dialysis and was the condition we used for stopped-flow analysis.

Using an osmotic gradient of 100 mM sucrose, the proteoliposomes with LPRs ranging from 90 to 10 showed an increased rate of water efflux compared to empty lipid vesicles as measured by scattered light. This reflects the increased number of AQPs inserted in the proteoliposome. Blocking HsAQP8 in the LPR 10 proteoliposomes with mercury showed an inhibition of the water channels by more than 40% compared to the non-blocked LPR 10 proteoliposomes (Fig. 2d). Since orientation of the protein during the vesicle formation is likely to be random, only AQPs oriented with their terminals facing the interior of the proteoliposome are affected by Hg^{2+} treatment (Fig. 1a) [63], and therefore total blockage was not expected. Our control vesicles with POPS/POPC lipids did not show any increase in light scattering due to diffusion of water across the lipid bilayer as seen e.g. for *E. coli* liposomes. This could be explained by the properties of the POPS/POPC lipids forming a tighter bilayer.

The position of the LE2 Arg in the ar/R region of HsAQP8 may influence the transport efficiency of water as has been suggested for PfAQP [26]. The precise orientation of LE2 Arg may be influenced by the structurally adjacent amino acid residues. For most aquaporins (see Table 2), it has been proposed that the amino acid residue next to the Arg (LE3 in Table 2 and Fig. 1a) anchors a specific residue in loop C (LC in Table 2 and Fig. 1a) via a hydrogen bond [64]. Although conserved in most aquaporins, this is not possible in AQP8 since the corresponding residues are Ala and Thr. Comparing our results to Liu et al. [31], differences are observed in the rate constants for HsAQP8. Liu et al. [31] report a rate constant of 59.03 s^{-1} at LPR 50 and 4.90 s^{-1} for control vesicles. This needs to be compared with our experiment at LPR 60, where we measured a rate constant of 1.5 s^{-1}. The reason for this discrepancy might be explained by methodological differences such as differently designed protein tags, different heterologous expression systems, differences in the size of the proteoliposomes and therefore different surface-to-volume ratios, and differences in osmotic gradients. Liu et al. [31] report a total blockage of water transport by 1 mM of Hg^{2+}. This was not expected due to the presumable random insertion of the aquaporin in the lipid bilayer of the proteoliposomes, seen with other AQPs [20], and the one-sided blocking by Hg^{2+}acting on a conserved Cys residue at the extracellular entrance of the pore. However, the choice of lipids for making the proteoliposomes could explain why we get a 50% inhibition by mercury while Liu et al. [31] get a 100% inhibition. The former level of inhibition is in accordance with a random (fifty–fifty) orientation after insertion of the protein and the latter with a single orientation of the protein (100% external side out) or, alternatively, with proteoliposomes permeable to mercury. There are examples demonstrating a single orientation of membrane proteins when inserted in proteoliposomes, which could suggest a single orientation in the study by Liu et al. [31].

4.7. 2D crystallization and analysis of HsAQP8

When reconstituted in neutral phosphatidyl lipids, HsAQP8 formed ordered 2D crystals (Fig. 3). Crystalline sheets were found in the presence of EDTA, at pH 7.0 and LPR 0.25–0.30. Often, addition of Mg^{2+} to the crystallization buffer, either in the form of $MgCl_2$ or as $MgSO_4$, improved the quality of His-tagged aquaporin crystals [17]. Here, addition of Mg^{2+} to the crystallization buffer resulted in protein aggregation. In contrast, addition of a chelating agent (EDTA) resulted in large fractions of well-ordered sheets. Elimination of divalent and trivalent cations from the crystallization buffer has an influence on the membrane surface charge by changing the phosphocholine (PC) and phosphoethanolamine (PE) dipoles [65], which appeared to facilitate crystal formation. Screening for the best crystallization conditions (Table 1) led to the conclusion that a change of temperature, after the appropriate time, from room temperature to 37 °C, has a significant influence on the formation of crystalline HsAQP8 arrays. Highly ordered sheets were predominantly found when the temperature was increased at later stages of the crystallization process.

4.8. Analysis of crystal packing arrangements

While highly ordered regions were found in single-layered HsAQP8 crystals that allowed the projection map to be calculated to a resolution of 8 Å (Fig. 3f), these regions were too small for electron diffraction. We suspected that the C-terminal 27 amino acid long extension might interfere with dense packing of the HsAQP8 tetramers and thus the formation of large, coherent 2D crystals. Therefore, they were exposed during crystallization to Lys-C protease in an attempt to improve packing regularity and crystal size. In the 283 amino

acid sequence of HsAQP8, seven possible Lys-C cleavage positions were found (Fig. 1a). When the protein is embedded in a lipid bilayer six Lys could be exposed to enzymatic cleavage whereas one Lys located in transmembrane helix 3 is likely to be inaccessible for the enzyme. Digestion by Lys-C, added after 36 h of crystallization, yielded large coherent crystals (Fig. 3e) that diffracted the electron beam up to 3 Å resolution (Fig. 3k). Taking the unit cell dimensions of a = b = 136 Å and the fact that one unit cell houses 4 tetramers per layer yields an area of 4624 Å^2 per tetramer. Compared to the unit cell of the unprocessed HsAQP8 2D crystal having a = b = 72 Å, i.e., 5184 Å^2 per tetramer, the packing density is 12% higher in the Lys-C treated HsAQP8 crystal.

SDS-PAGE analysis showed that upon Lys-C treatment of crystals parts of both the N-terminal and the C-terminal region are removed (Fig. 4). A peptide of 11 amino acids is released from the N-terminal with at least 20% efficiency and a peptide of either 18 or 29 amino acids is released from the C-terminal with about 80% efficiency. In agreement with this the prominent peripheral domain seen in the projection map of the unprocessed crystal (Fig. 3f) is reduced in the correlation average of a Lys-C treated crystal (Fig. 3h). Therefore, different crystal contacts emerged that allows tetramers to be more tightly packed. The cleavage site is most likely at K254 since the shift in molecular weight corresponds to a total of 29 plus 11 amino acids form the N-terminus, i.e. a loss of 4.4 kDa. Additional cleavage in helix 3, in the second cytosolic loop (i.e. loop D) and at K248 in the C-terminal region could not be discerned.

Although Lys-C treated HsAQP8 crystals diffracted to high resolution, they exhibited a disturbing disorder reflected by systematically smeared diffraction orders. The pattern created by this disorder resulted in lines of density extending over two lattice spacings parallel to the lattice lines, indicating that the disorder happens along lattice lines. Using the correlation averaging approach [55] a projection map was obtained that exhibited 'cornerstones', i.e. distinct tetramers whose morphology was best modeled by the sum of two tetramers sharing their 4-fold symmetry axis, but apposed in opposite orientations (Fig. 3g). It appears that the interactions holding these octameric 'cornerstones' together are rather strong. From Fourier filtered images (Fig. 3i) rows of tetramers between these 'cornerstones' appeared to be less ordered. Because shifts of such intermediate tetramers can occur along both directions of the orthogonal lattice, the disorder manifests itself as lines in the diffraction patterns (Fig. 3k, asterisk).

In conclusion, we show the overexpression, purification, functional reconstitution and 2D crystallization of human AQP8. By using different crystallization methods and conditions, highly ordered crystalline sheets were obtained. These results constitute a step towards solving the high-resolution structure of a unique human aquaporin that in pore structure and substrate specificity differ substantially from other human aquaporins.

Supplementary materials related to this article can be found online at doi:10.1016/j.bbamem.2011.12.006.

Acknowledgements

We thank Adine Karlsson for technical assistance, Nora Eifler for making the class average of the single particles and for help with the stopped-flow measurements and Maria Ekerot for help with the expression system. This work was supported by the Swedish Research Council (VR), the Research Council Formas, the Research School in Pharmaceutical Sciences (FLÄK), the Research School in Molecular Protein Science, the Royal Physiographical Society and the Bokelunds Traveling Grant, the Swiss National Foundation (grant 3100A0-108299/2 to AE), the National Center of Competence in Structural Biology, and a Marie Curie Fellowship to JK in the program EMBNTrain (MSCF-CT-2005-029458).

References

[1] G.M. Preston, T.P. Carroll, W.B. Guggino, P. Agre, Appearance of water channels in *Xenopus* oocytes expressing red cell CHIP28 protein, Science 256 (1992) 385–387.
[2] K. Ishibashi, M. Kuwahara, Y. Gu, Y. Kageyama, A. Tohsaka, F. Suzuki, F. Marumo, S. Sasaki, Cloning and functional expression of a new water channel abundantly expressed in the testis permeable to water, glycerol, and urea, J. Biol. Chem. 272 (1997) 20782–20786.
[3] G.P. Bienert, M. Thorsen, M.D. Schussler, H.R. Nilsson, A. Wagner, M.J. Tamas, T.P. Jahn, A subgroup of plant aquaporins facilitate the bi-directional diffusion of As(OH)3 and Sb(OH)3 across membranes, BMC Biol. 6 (2008) 26.
[4] J. Takano, M. Wada, U. Ludewig, G. Schaaf, N. von Wiren, T. Fujiwara, The *Arabidopsis* major intrinsic protein NIP5;1 is essential for efficient boron uptake and plant development under boron limitation, Plant Cell 18 (2006) 1498–1509.
[5] J.F. Ma, K. Tamai, N. Yamaji, N. Mitani, S. Konishi, M. Katsuhara, M. Ishiguro, Y. Murata, M. Yano, A silicon transporter in rice, Nature 440 (2006) 688–691.
[6] L.S. King, D. Kozono, P. Agre, From structure to disease: the evolving tale of aquaporin biology, Nat. Rev. Mol. Cell Biol. 5 (2004) 687–698.
[7] A.S. Verkman, Mammalian aquaporins: diverse physiological roles and potential clinical significance, Expert Rev. Mol. Med. 10 (2008) e13.
[8] B. Yang, Y. Song, D. Zhao, A.S. Verkman, Phenotype analysis of aquaporin-8 null mice, Am. J. Physiol. Cell Physiol. 288 (2005) C1161–C1170.
[9] K. Murata, K. Mitsuoka, T. Hirai, T. Walz, P. Agre, J.B. Heymann, A. Engel, Y. Fujiyoshi, Structural determinants of water permeation through aquaporin-1, Nature 407 (2000) 599–605.
[10] D. Fu, A. Libson, L.J. Miercke, C. Weitzman, P. Nollert, J. Krucinski, R.M. Stroud, Structure of a glycerol-conducting channel and the basis for its selectivity, Science 290 (2000) 481–486.
[11] B.L. de Groot, H. Grubmuller, The dynamics and energetics of water permeation and proton exclusion in aquaporins, Curr. Opin. Struct. Biol. 15 (2005) 176–183.
[12] H. Sui, B.G. Han, J.K. Lee, P. Walian, B.K. Jap, Structural basis of water-specific transport through the AQP1 water channel, Nature 414 (2001) 872–878.
[13] J.S. Jung, G.M. Preston, B.L. Smith, W.B. Guggino, P. Agre, Molecular structure of the water channel through aquaporin CHIP. The hourglass model, J. Biol. Chem. 269 (1994) 14648–14654.
[14] T. Gonen, P. Sliz, J. Kistler, Y. Cheng, T. Walz, Aquaporin-0 membrane junctions reveal the structure of a closed water pore, Nature 429 (2004) 193–197.
[15] T. Gonen, Y. Cheng, P. Sliz, Y. Hiroaki, Y. Fujiyoshi, S.C. Harrison, T. Walz, Lipid–protein interactions in double-layered two-dimensional AQP0 crystals, Nature 438 (2005) 633–638.
[16] W.E. Harries, D. Akhavan, L.J. Miercke, S. Khademi, R.M. Stroud, The channel architecture of aquaporin 0 at a 2.2-A resolution, Proc. Natl. Acad. Sci. U. S. A. 101 (2004) 14045–14050.
[17] A.D. Schenk, P.J. Werten, S. Scheuring, B.L. de Groot, S.A. Muller, H. Stahlberg, A. Philippsen, A. Engel, The 4.5A structure of human AQP2, J. Mol. Biol. 350 (2005) 278–289.
[18] Y. Hiroaki, K. Tani, A. Kamegawa, N. Gyobu, K. Nishikawa, H. Suzuki, T. Walz, S. Sasaki, K. Mitsuoka, K. Kimura, A. Mizoguchi, Y. Fujiyoshi, Implications of the aquaporin-4 structure on array formation and cell adhesion, J. Mol. Biol. 355 (2006) 628–639.
[19] J.D. Ho, R. Yeh, A. Sandstrom, I. Chorny, W.E. Harries, R.A. Robbins, L.J. Miercke, R.M. Stroud, Crystal structure of human aquaporin 4 at 1.8 A and its mechanism of conductance, Proc. Natl. Acad. Sci. U. S. A. 106 (2009) 7437–7442.
[20] R. Horsefield, K. Norden, M. Fellert, A. Backmark, S. Tornroth-Horsefield, A.C. Terwisscha van Scheltinga, J. Kvassman, P. Kjellbom, U. Johanson, R. Neutze, High-resolution X-ray structure of human aquaporin 5, Proc. Natl. Acad. Sci. U. S. A. 105 (2008) 13327–13332.
[21] W. Kukulski, A.D. Schenk, U. Johanson, T. Braun, B.L. de Groot, D. Fotiadis, P. Kjellbom, A. Engel, The 5A structure of heterologously expressed plant aquaporin SoPIP2;1, J. Mol. Biol. 350 (2005) 611–616.
[22] S. Törnroth-Horsefield, Y. Wang, K. Hedfalk, U. Johanson, M. Karlsson, E. Tajkhorshid, R. Neutze, P. Kjellbom, Structural mechanism of plant aquaporin gating, Nature 439 (2006) 688–694.
[23] D.F. Savage, P.F. Egea, Y. Robles-Colmenares, J.D. O'Connell III, R.M. Stroud, Architecture and selectivity in aquaporins: 2.5 A X-ray structure of aquaporin Z, PLoS Biol. 1 (2003) E72.
[24] J. Jiang, B.V. Daniels, D. Fu, Crystal structure of AqpZ tetramer reveals two distinct Arg-189 conformations associated with water permeation through the narrowest constriction of the water-conducting channel, J. Biol. Chem. 281 (2006) 454–460.
[25] J.K. Lee, D. Kozono, J. Remis, Y. Kitagawa, P. Agre, R.M. Stroud, Structural basis for conductance by the archaeal aquaporin AqpM at 1.68 A, Proc. Natl. Acad. Sci. U. S. A. 102 (2005) 18932–18937.
[26] Z.E. Newby, J. O'Connell III, Y. Robles-Colmenares, S. Robles-Colmenares, L.J. Miercke, R.M. Stroud, Crystal structure of the aquaglyceroporin PfAQP from the malarial parasite *Plasmodium falciparum*, Nat. Struct. Mol. Biol. 15 (2008) 619–625.
[27] G. Fischer, U. Kosinska-Eriksson, C. Aponte-Santamaria, M. Palmgren, C. Geijer, K. Hedfalk, S. Hohmann, B.L. de Groot, R. Neutze, K. Lindkvist-Petersson, Crystal structure of a yeast aquaporin at 1.15 Angstrom reveals a novel gating mechanism, PLoS Biol. 7 (2009) e1000130.
[28] R. Grisshammer, Understanding recombinant expression of membrane proteins, Curr. Opin. Biotechnol. 17 (2006) 337–340.
[29] S. Wagner, M.L. Bader, D. Drew, J.W. de Gier, Rationalizing membrane protein overexpression, Trends Biotechnol. 24 (2006) 364–371.
[30] T. Warne, M.J. Serrano-Vega, J.G. Baker, R. Moukhametzianov, P.C. Edwards, R. Henderson, A.G. Leslie, C.G. Tate, G.F. Schertler, Structure of a beta1-adrenergic G-protein-coupled receptor, Nature 454 (2008) 486–491.

[31] K. Liu, H. Nagase, C.G. Huang, G. Calamita, P. Agre, Purification and functional characterization of Aquaporin-8, Biol. Cell 98 (2006) 153–161.
[32] L.M. Holm, T.P. Jahn, A.L. Moller, J.K. Schjoerring, D. Ferri, D.A. Klaerke, T. Zeuthen, NH3 and $NH4^+$ permeability in aquaporin-expressing Xenopus oocytes, Pflugers Arch. 450 (2005) 415–428.
[33] T.P. Jahn, A.L. Moller, T. Zeuthen, L.M. Holm, D.A. Klaerke, B. Mohsin, W. Kuhlbrandt, J.K. Schjoerring, Aquaporin homologues in plants and mammals transport ammonia, FEBS Lett. 574 (2004) 31–36.
[34] S.M. Saparov, K. Liu, P. Agre, P. Pohl, Fast and selective ammonia transport by aquaporin-8, J. Biol. Chem. (2007).
[35] G.P. Bienert, A.L. Moller, K.A. Kristiansen, A. Schulz, I.M. Moller, J.K. Schjoerring, T.P. Jahn, Specific aquaporins facilitate the diffusion of hydrogen peroxide across membranes, J. Biol. Chem. 282 (2007) 1183–1192.
[36] N. Koyama, K. Ishibashi, M. Kuwahara, N. Inase, M. Ichioka, S. Sasaki, F. Marumo, Cloning and functional expression of human aquaporin8 cDNA and analysis of its gene, Genomics 54 (1998) 169–172.
[37] D. Ferri, A. Mazzone, G.E. Liquori, G. Cassano, M. Svelto, G. Calamita, Ontogeny, distribution, and possible functional implications of an unusual aquaporin, AQP8, in mouse liver, Hepatology 38 (2003) 947–957.
[38] G. Calamita, D. Ferri, P. Gena, G.E. Liquori, A. Cavalier, D. Thomas, M. Svelto, The inner mitochondrial membrane has aquaporin-8 water channels and is highly permeable to water, J. Biol. Chem. 280 (2005) 17149–17153.
[39] L.R. Soria, E. Fanelli, N. Altamura, M. Svelto, R.A. Marinelli, G. Calamita, Aquaporin-8-facilitated mitochondrial ammonia transport, Biochem. Biophys. Res. Commun. 393 (2010) 217–221.
[40] B. Yang, D. Zhao, A.S. Verkman, Evidence against functionally significant aquaporin expression in mitochondria, J. Biol. Chem. 281 (2006) 16202–16206.
[41] J.D. Thompson, D.G. Higgins, T.J. Gibson, CLUSTAL W: improving the sensitivity of progressive multiple sequence alignment through sequence weighting, position-specific gap penalties and weight matrix choice, Nucleic Acids Res. 22 (1994) 4673–4680.
[42] J.B. Heymann, A. Engel, Structural clues in the sequences of the aquaporins, J. Mol. Biol. 295 (2000) 1039–1053.
[43] D. Swofford, PAUP*: Phylogenetic Analysis Using Parsimony (*and Other Methods), 4.0b10 Edition, Sinnauer Associates, Sunderland, MA, 2000.
[44] M. Karlsson, D. Fotiadis, S. Sjovall, I. Johansson, K. Hedfalk, A. Engel, P. Kjellbom, Reconstitution of water channel function of an aquaporin overexpressed and purified from *Pichia pastoris*, FEBS Lett. 537 (2003) 68–72.
[45] U.K. Laemmli, Cleavage of structural proteins during the assembly of the head of bacteriophage T4, Nature 227 (1970) 680–685.
[46] J.C. Bearden Jr., Quantitation of submicrogram quantities of protein by an improved protein-dye binding assay, Biochim. Biophys. Acta 533 (1978) 525–529.
[47] E. Gasteiger, C. Hoogland, A. Gattiker, S. Duvaud, M.R. Wilkins, R.D. Appel, A. Bairoch, Protein identification and analysis tools on the ExPASy Server, the proteomics protocols handbook, Hum. Press (2005) 571–607.
[48] S.C. Gill, P.H. von Hippel, Calculation of protein extinction coefficients from amino acid sequence data, Anal. Biochem. 182 (1989) 319–326.
[49] B.K. Jap, M. Zulauf, T. Scheybani, A. Hefti, W. Baumeister, U. Aebi, A. Engel, 2D crystallization: from art to science, Ultramicroscopy 46 (1992) 45–84.
[50] T. Hirai, K. Murata, K. Mitsuoka, Y. Kimura, Y. Fujiyoshi, Trehalose embedding technique for high-resolution electron crystallography: application to structural study on bacteriorhodopsin, J. Electron. Microsc. (Tokyo) 48 (1999) 653–658.
[51] S.J. Ludtke, P.R. Baldwin, W. Chiu, EMAN: semiautomated software for high-resolution single-particle reconstructions, J. Struct. Biol. 128 (1999) 82–97.
[52] B. Gipson, X. Zeng, H. Stahlberg, 2dx_merge: data management and merging for 2D crystal images, J. Struct. Biol. 160 (2007) 375–384.
[53] A. Philippsen, A.D. Schenk, G.A. Signorell, V. Mariani, S. Berneche, A. Engel, Collaborative EM image processing with the IPLT image processing library and toolbox. J. Struct. Biol. 157 (207) 28–37.
[54] R. Zardoya, Phylogeny and evolution of the major intrinsic protein family, Biol. Cell 97 (2005) 397–414.
[55] W.O. Saxton, W. Baumeister, The correlation averaging of a regularly arranged bacterial cell envelope protein, J. Microsc. 127 (1982) 127–138.
[56] B. Gipson, X. Zeng, Z.Y. Zhang, H. Stahlberg, 2dx–user-friendly image processing for 2D crystals, J. Struct. Biol. 157 (2007) 64–72.
[57] S.B. Hedges, J.E. Blair, M.L. Venturi, J.L. Shoe, A molecular timescale of eukaryote evolution and the rise of complex multicellular life, BMC Evol. Biol. 4 (2004) 2.
[58] M. Opekarova, W. Tanner, Specific lipid requirements of membrane proteins—a putative bottleneck in heterologous expression, Biochim. Biophys. Acta 1610 (2003) 11–22.
[59] K. Hedfalk, N. Pettersson, F. Oberg, S. Hohmann, E. Gordon, Production, characterization and crystallization of the *Plasmodium falciparum* aquaporin, Protein Expr. Purif. 59 (2008) 69–78.
[60] L. Hasler, T. Walz, P. Tittmann, H. Gross, J. Kistler, A. Engel, Purified lens major intrinsic protein (MIP) forms highly ordered tetragonal two-dimensional arrays by reconstitution, J. Mol. Biol. 279 (1998) 855–864.
[61] J. Kistler, K. Goldie, P. Donaldson, A. Engel, Reconstitution of native-type noncrystalline lens fiber gap junctions from isolated hemichannels, J. Cell Biol. 126 (1994) 1047–1058.
[62] D. Fotiadis, P. Jeno, T. Mini, S. Wirtz, S.A. Muller, L. Fraysse, P. Kjellbom, A. Engel, Structural characterization of two aquaporins isolated from native spinach leaf plasma membranes, J. Biol. Chem. 276 (2001) 1707–1714.
[63] G.M. Preston, J.S. Jung, W.B. Guggino, P. Agre, The mercury-sensitive residue at cysteine 189 in the CHIP28 water channel, J. Biol. Chem. 268 (1993) 17–20.
[64] J.A. Danielson, U. Johanson, Unexpected complexity of the aquaporin gene family in the moss *Physcomitrella patens*, BMC Plant Biol. 8 (2008) 45.
[65] J. Seelig, P.M. Macdonald, P.G. Scherer, Phospholipid head groups as sensors of electric charge in membranes, Biochemistry 26 (1987) 7535–7541.
[66] R. Henderson, J.M. Baldwin, K.H. Downing, J. Lepault, F. Zemlin, Structure of purple membrane from halobacterium halobium: recording, measurement and evaluation of electron micrographs at 3.5 Å resolution, Ultramicroscopy 19 (1986) 147–178.